RSC Advances

ROYAL SOCIETY OF CHEMISTRY

www.rsc.org/advances

Catalytic combustion of soot over Ce and Co substituted three-dimensionally ordered macroporous $La_{1-x}Ce_xFe_{1-y}Co_yO_3$ perovskite catalysts

Nengjie Feng, Yang Wu, Jie Meng, Chong Chen, Lei Wang*, Hui Wan, Guofeng Guan*

State Key Laboratory of Materials-Oriented Chemical Engineering, College of Chemical Engineering, Nanjing Tech University, Nanjing 210009, PR China

*Corresponding author, telephone: +86-25-83587198. E-mail: wanglei@njtech.edu.cn; guangf@njtech.edu.cn

Abstract:

Three-dimensionally ordered macroporous (3DOM) $La_{1-x}Ce_xFe_{1-y}Co_yO_3$ (x=0-0.4, y=0-0.6) perovskite catalysts were successfully prepared by colloidal crystal templating method and employed for soot combustion. The morphology, structure, and redox property of the catalysts were characterized by XRD, FT-IR, SEM, BET, UV-Vis DRS, XPS, O_2-TPD and H_2-TPR techniques, and the catalytic activities for soot combustion were evaluated by TPO device using NO/O_2 as oxidant. Co-substitution at Fe-site of 3DOM $LaFeO_3$ perovskites can effectively enhance the catalytic activity, however, the 3DOM structure is partly destroyed that restricts the further improvement of the activity. The appropriate doping of Ce in La-site can lower the solidification temperature of precursors, and thus the damage of structure can be avoided. Additionally, the reducibility and surface adsorbed oxygen species of the catalyst are also improved as revealed by H_2-TPR, O_2-TPD and XPS. Whereas with an excess of Ce substitution, Co_3O_4 and CeO_2 impurities will generate and grow as demonstrated by XRD and

FT-IR. Among all the catalysts, 3DOM $La_{0.7}Ce_{0.3}Fe_{0.4}Co_{0.6}O_3$ perovskite with well-ordered macroporous structure possesses the highest activity for soot combustion.

1. Introduction

Soot particles emitted by diesel engines are known to be hazardous to the environment.[1] To date, the particle emission still cannot be efficiently reduced only through the engine modification, and thus more attention has been paid to the catalytic after treatment processes, especially the catalysts in them.[2] Various kinds of catalysts, which have high catalytic activities, have been used for soot removal, such as noble metals, alkali metal containing catalysts, spinel and perovskite-type oxides.[3, 4] Among them, supported noble metal catalysts have been widely used for soot combustion for their excellent catalytic activities at low temperatures.[5-7] However, the limited resources of the reserves and the high cost often restrict their widespread applications. In the past decades, perovskite-type catalyst, with the general formula of ABO_3, has drawn much attention due to its considerable catalytic performance, much lower price, and higher chemical/thermal/structural stability.[8-10] The catalytic activity of perovskite mainly depends on B-site cation, and suffers from the influence of A-site cation indirectly.[11, 12] When A-site or B-site ions in perovskites are partly substituted by other ions, the catalytic activity for soot combustion will improve.[13] The perovskite-type catalysts are regarded as potential substitutes for noble metal catalysts for soot removal.[14]

In recent years, three-dimensionally ordered macroporous (3DOM) perovskites have been reported to show better activity for soot combustion, owing to the interpenetrating well-ordered macroporous structure.[15-18] This structure allows the soot particles to enter the

inner pores of catalysts without resistance, and thus providing more opportunities for soot particles to reach the active sites. So far, various kinds of 3DOM perovskites have been successfully prepared by the colloidal crystal templating method.[14, 15, 19] Among them, 3DOM $LaFeO_3$ perovskites are widely applied and easy to prepare for the low solidification temperature of Fe.[16, 20-22] Unfortunately, the activity of $LaFeO_3$ for soot combustion was lower than that of $LaCoO_3$ and $LaMnO_3$.[9] The introduction of Co into the 3DOM $LaFeO_3$ can improve the activity obviously, while large amounts of Co will seriously destroy the 3DOM structure during calcination.[23] Hence, it is a big challenge to prepare the Fe-based perovskites both with the well-ordered 3DOM structure and the high activity for soot combustion. In order to successfully prepare 3DOM structure oxides, the solidification temperature of metal precursors must be lower than the glass-transition temperature (T_g) of polymer templates.[22] The doping of Co into the 3DOM $LaFeO_3$ perovskites can increase the solidification temperature of metal precursor. For this reason, the polymer template will fuse and distort before the solidification of metal precursor and thus the well-ordered 3DOM structure cannot form. Ce is suitable to construct the 3DOM structure for its relatively low solidification temperature.[22] And until now, different kinds of Ce-based catalysts have shown good activity for soot removal.[24-27] The further substitution of Ce at La-site will lower the average solidification temperature of the precursor, so the metal precursor will solidify before the polymer templates melt and distort, and the destruction of 3DOM structure during calcination may be avoided. However, the substitution of A-site La by Ce in the 3DOM perovskites have rarely been discussed. The appropriate doping of Ce can avoid the destruction of 3DOM structure, meanwhile the redox properties and the catalytic activities of the catalysts will be

further improved.[28-30] Therefore, 3DOM $LaFeO_3$ perovskites with simultaneous substitution of both A and B-site ions by Ce and Co with well-ordered macroporous structure and high activity for soot removal are attainable.

In this work, a series of Ce/Co simultaneously substituted 3DOM perovskite catalysts $La_{1-x}Ce_xFe_{1-y}Co_yO_3$ (x=0-0.4, y=0-0.6) were prepared by colloidal crystal templating method. The XRD, FT-IR, SEM, BET, XPS, H_2-TPR, O_2-TPD and UV-Vis DRS techniques were performed to investigate the influences of Ce/Co-doping on morphology, structure, and redox ability of the catalysts. The catalytic performance for soot combustion was also discussed in detail.

2. Experiment

2.1 Catalyst preparation.

Three-dimensionally ordered macroporous $La_{1-x}Ce_xFe_{1-y}Co_yO_3$ (x=0-0.4, y=0-0.6) perovskites were synthesized using colloidal crystal template method. The well-arrayed PMMA hard template with an average diameter of 375 nm was prepared according to the literatures[16, 19] and chosen as the colloidal crystal template. The mixed metal solutions were made by the corresponding nitrate salts dissolved in the ethylene glycol-methanol (40 vol%) solution after stirring for 2 h, and the molar of the total metal ions in the mix solution was 2 mol/L. Then, the PMMA colloidal crystal template was immersed into the solution for about 4 h to ensure permeation of the precursor solution into the voids between the PMMA spheres. Excess solution was removed through vacuum filtration. After drying in oven at 40 ^oC overnight, the sample was placed into a porcelain boat and calcined to remove the template in a tube furnace under air flow. The temperature was raised at the rate of 1 ^oC/min from 50 ^oC to

650 ^{o}C and kept at this temperature for another 5 h.

For comparison, $La_{1-x}Ce_xFe_{1-y}Co_yO_3$ catalysts without macroporous structure were also prepared by the citric acid complexation method.[8] Each time, the corresponding nitrate salts were dissolved in deionized water to obtain an aqueous solution of La^{3+}, Ce^{3+}, Co^{2+}, and Fe^{3+} with the expected stoichiometry. The molar ratio of citric acid to total metal ions was 1.1:1. The resulting solutions were evaporated to dryness at 80 °C with vigorous stirring. The clear solution gradually turned into sol and finally transformed into gel. At last, the wet gel was dried at 110 °C for 12 h and calcinated at 650 °C for 5 h.

2.2. Catalyst characterization.

The scanning electron microscopy (SEM) images were observed on a Hitachi S4800 field-emission SEM instrument operated at 5 kV. X-ray diffraction (XRD) patterns of the crystal structures for the catalysts were recorded in a SmartLab-9 Japan automated power X-ray diffraction meter operating at 100 mA and 40 kV using Cu Kα as radiation source (λ=0.1541 nm). The scanning range of 2θ was from 10 to 80° with a step size of 0.02°. N_2 adsorption-desorption measurements were carried out on a Micromeritics ASAP 2020 system model instrument at -196 °C. Prior to measurement, the samples were degassed at 300 °C under vacuum for 4 h. Brunauer-Emmett-Teller (BET) method was used to measure the specific surface areas. Fourier transform infrared (FT-IR) spectroscopy was carried out on a Thermo Nicolet 870 spectrophotometer in the range of 400-1200 cm^{-1} with anhydrous KBr as dispersing agent. X-ray photoelectron spectroscopy (XPS) spectra were recorded on a PHI-5000 spectrometer using Al Kα (1486.6 eV) radiation as the excitation source. All binding energies were referenced to the C 1s peak at 284.5 eV, and Gaussian-Lorentzian and

Shirley background was applied for peak analysis. The UV-Vis diffuse reflectance spectroscopy (UV-Vis DRS) experiments were performed on a UV-Vis spectrophotometer (PerkinElmer Lambda 950). Temperature-programmed reduction (TPR) was conducted on a BEL-CAT (JAPAN InC.) chemisorption analyser equipped with a TCD detector. Each time, 30 mg sample was pretreated in Ar stream at 200 ^{o}C for 2 h, and then cooled down to room temperature. 10% H_2/Ar at a total flow rate 40 mL/min flowed over the sample from room temperature to 900 ^{o}C with a heating rate of 10 ^{o}C/min. O_2-Temperature-programmed desorption (O_2-TPD) was also conducted on a Micromeritics AutoChem II 2920 chemical adsorption analyser. Each time, 30 mg sample (40-60 mesh) was pretreated in Ar stream at 200 ^{o}C for 2 h, and then cooled down to room temperature. Then, O_2 was absorbed at 70 ^{o}C for 2 h using a mixture gas of 3% O_2/Ar, and subsequently the sample was purged by a flowing pure He stream to remove excessive and weakly adsorbed O_2. Finally, the sample was heated to 900 ^{o}C with heating rate of 10 ^{o}C/min in a pure He flow and desorption pattern was recorded.

2.3. Activity testing.

The continuous fixed-bed reactor was also used to evaluate the activity of the catalysts under the loose contact. During each experiment, 20 mg soot (Printex-U from Degussa) was mixed with 180 mg catalyst using a spatula to obtain a loose contact. The mixture was placed into the quartz tube (i.d. = 14 mm) and heated from 200 to 650 °C (2 °C/min) in a flow of 500 ppm NO, 5 vol% O_2, and the balanced N_2 with a rate of 100 mL/min. The outlet gas compositions were analyzed by the infrared gas analyser (Infralyt 50). The conversion rate of soot at one temperature (Cs:t) was defined as the sum of CO concentrations (Cco) and CO_2

concentrations (Cco_2) from 200 °C to this temperature (t) divided by the sum of the CO and CO_2 concentrations from 200 °C to 650 °C; i.e., $Cs{:}t=\frac{\int_{200}^{t}(Cco+Cco_2)}{\int_{200}^{650}(Cco+Cco_2)}$. In this work, the temperatures when the conversion rate of soot reached 10%, 50%, and 90% were denoted as T_{10}, T_{50}, and T_{90}. The selectivity of CO_2 at the temperature, when the soot-burnt rate was the highest, was denoted as S_{CO2}^{m}. All these results were used to evaluate catalytic performance of the catalysts.

For comparison, soot combustion experiment in the absence of NO and NO oxidation experiment were also carried out. NO oxidation experiment was carried out in a fixed-bed reactor. Each time, 180 mg catalyst and no soot was used for this reaction. The catalyst was placed into the quartz tube (i.d. = 14 mm) and heated from 200 to 650 °C (2 °C/min) with reactant gas in a rate of 100 mL/min. Reactant gas compositions were 5% O_2 and 500 ppm NO with N_2 balanced gas. The outlet NO_2 concentration was analyzed by the infrared gas analyser (Infralyt 50).

3. Results and discussion

3.1. Catalysts characterization.

Figure 1 shows the morphology of all catalysts prepared by colloidal crystal templating method. For $LaFeO_3$ catalyst, the "inverse-opal" skeletons[15] surrounded by uniform close-packed periodic voids can be clearly observed, which indicates that the well-ordered macroporous structure has been successfully constructed. The average diameter of the newly formed pores is about 300 nm, which shrinks by 20% compared with the initial size of PMMA microspheres (375 nm). This shrinkage is due to the fusion of PMMA spheres and the

sintering of perovskites during calcination, however the ordered and uniform structure has not been damaged by this shrinkage.[14, 31] After the introduction of Co, some skeletons of the 3DOM structure fracture and the macroporous structure is destroyed to some extent. This is because the solidification temperature of Co (113 ^{o}C) is much higher than that of Fe (55 ^{o}C), and also higher than the glass transition temperature of PMMA templates (109 ^{o}C).[22] In other words, the average solidification temperature of the Co-doped precursor increases, which is unfavorable to the formation of 3DOM structure.[14, 22] When the substitution amount of Co reaches 0.6, the average solidification temperature of precursor is too high that the catalysts can hardly maintain the 3DOM structure. In comparison, the further doping of Ce into $LaFe_{0.4}Co_{0.6}O_3$ perovskite efficiently avoids the collapse of macroporous structure and improves the ordered degree of the macrostructure. The introduction of Ce in A-site decreases the average solidification temperature of the precursor owing to lower solidification temperature of Ce (110 ^{o}C) than that of La (130 ^{o}C), and thus the well-ordered 3DOM structure will reappear. When the doping amount of Ce reaches 0.2 or more, the perovskite catalysts with intact 3DOM structure can form.

The XRD patterns of 3DOM $La_{1-x}Ce_xFe_{1-y}Co_yO_3$ perovskite catalysts are shown in Figure 2(a), and the partial enlargement of XRD patterns ranging from 31.5 ^{o} to 33.5 ^{o} are shown in Figure 2(b). All the catalysts prepared by colloidal crystal templating method possess ABO_3 perovskite-type structure. It indicates that the calcination condition (650 ^{o}C for 5 h) is sufficient to format well-crystallized ABO_3 type perovskite structure. For $LaFe_{1-y}Co_yO_3$ catalysts, the perovskites exhibit only a single perovskite-type structure regardless of Co substitution level owing to the similar ionic radii of Co^{3+} and Fe^{3+} ions.[32] With the increasing

doping amount of Co, a slight shift to higher 2θ angles is also detected, which demonstrates that the Co has been incorporated into the lattice of perovskites successfully. After the addition of Ce, the intensity of diffraction peak decreases apparently, which implies that the substitution of Ce diminishes the crystallization degree of the catalysts.[29] Meanwhile, the diffraction peaks shift to lower 2θ positions with the gradual increase of Ce content, suggesting the successful incorporation of Ce into the lattice of perovskite. In addition, two new characteristic peaks corresponding to CeO_2 and Co_3O_4 appear at 28 ^{o} and 37 ^{o} when the doping amount of Ce is greater than 0.1. This is because the introduction of Ce into the perovskite may lead to the distortion of structure and the contraction of lattice, and as a result small amounts of CeO_2 and Co_3O_4 are separated from perovskite.[8, 29] The crystallite sizes, which calculate by Scherrer equation using the XRD data of the most prominent line, are listed in Table 1. The size of $LaFeO_3$ perovskite is 24.2 nm, and monotonously decreases to 22.9 nm with increasing Co substitution. When Ce is doped into the perovskite, the size of perovskite further reduces obviously. This is due to the dispersing effect of CeO_2 and Co_3O_4 impurity phases separated from the perovskites.[29]

The specific surface areas of the catalysts are also listed in Table 1. It can be found that all these values are relatively high even after high temperature treatment, which are attributed to their well-ordered macroporous structures. The large surface area of 3DOM perovskite is favorable to achieving the large number of contact points between the catalyst and soot particulates. The specific surface area of 3DOM $LaFeO_3$ is 21.7 m^2/g, and a decreasing tendency of the values is observed along with the increase of Co substitution content. The main reason is that the addition of Co influences the ordered degree of the macroporous

structures during the preparation.[14, 23] The fractured catalysts then accumulate together, leading to a decrease of the specific surface area. As shown in Figure 1(e), $LaFe_{0.4}Co_{0.6}O_3$ can hardly maintain the well-ordered macroporous structures with the lowest specific surface area of 18.5 m^2/g. Interestingly, after the introduction of Ce, the corresponding values increase to some extent, with a maximum of 22.5 m^2/g at 30% Ce substitution amount. It means that the further introduction of Ce restrains the collapse of 3DOM structure.

The FT-IR spectra of $La_{1-x}Ce_xFe_{1-y}Co_yO_3$ catalysts are given in Figure 3. There are two main characteristic bands in each samples. The absorption bands at 600 cm^{-1} are attributed to the Fe-O or Co-O stretching vibrations and the peaks around 400 cm^{-1} correspond to the O-Fe-O or O-Co-O deformation vibrations in the perovskites.[23, 28, 33] The FT-IR results further demonstrate that the ABO_3 perovskite structures are present and stable after substitution. When the content of Ce at A-site increases to 0.2, a new band phase at about 660 cm^{-1} related to the Co_3O_4 impurity is witnessed.[34] Furthermore, with the increasing doping amount of Ce, there is a slight increase in the intensity of the corresponding band. These results are consistent with those of the XRD.

3DOM $LaFeO_3$, $LaFe_{0.4}Co_{0.6}O_3$ and $La_{0.7}Ce_{0.3}Fe_{0.4}Co_{0.6}O_3$ are further characterized by using UV-Vis spectroscopy and the results are shown in Figure 4. UV-Vis DRS is a significant characterization to investigate the geometry of the metal centres existing in the material. As shown in Figure 4, all the three catalysts have ultraviolet absorption, which are ascribed to the electronic transitions from the valence band to conduction band owing to the octahedral coordination of oxygen around Fe in perovskite structure (O 2p→Fe 3d).[35, 36] However, the performance of visible light absorption is improved as a result of doping Co. It

is mainly due to the presence of Co^{2+} in the tetrahedral and the Co^{3+} in the octahedral position, which proves that Co ions have been successfully incorporated into the perovskite structure.[37, 38] Since some absorption peaks of Ce are overlapped, the further introduction of Ce has little impact on the DRS spectra.

Figure 5 shows the Ce 3d and Co 2p spectra of the 3DOM $La_{1-x}Ce_xFe_{0.4}Co_{0.6}O_3$ ($0 \le x \le 0.4$) perovskite. As shown in Figure 5A, all the Ce-containing samples show two multiplets corresponding to the Ce $3d_{3/2}$ (u) and Ce $3d_{5/2}$ (v) levels. The binding energy peaks u''', u'', u, v''', v'' and v respectively located at about 916.0, 906.8, 900.1, 897.4, 888.3 and 881.7 eV are all belong to tetravalent Ce with different electron configuration states.[39, 40] With Ce content increasing, no obvious change, other than the increasing intensity of these binding energy peaks, is found in the spectra. It can be concluded that the main valence state of Ce in the 3DOM $La_{1-x}Ce_xFe_{0.4}Co_{0.6}O_3$ ($0 \le x \le 0.4$) perovskite is tetravalence. It is mainly due to the better stability of Ce^{4+} than Ce^{3+} during high temperature calcination. As shown in Figure 5B, two peaks corresponding to Co $2p_{1/2}$ and Co $2p_{3/2}$ are detected in 3DOM $La_{1-x}Ce_xFe_{0.4}Co_{0.6}O_3$ ($0 \le x \le 0.4$) catalysts. The peak binding energy of Co $2p_{3/2}$ for $LaFe_{0.4}Co_{0.6}O_3$ is 779.6 eV, which is similar to that of Co_2O_3 reported in literature.[41] It indicates that the main valence of Co ions in $LaFe_{0.4}Co_{0.6}O_3$ is trivalent. With the increase of Ce substitution, slight shifts in the binding energies of Co $2p_{3/2}$ are found. The peak of Co $2p_{3/2}$ firstly moves from 779.6 eV to 780.3 eV ($La_{0.8}Ce_{0.2}Fe_{0.4}Co_{0.6}O_3$), which means part of Co^{3+} have changed into Co^{2+} to maintain the electronic balance when Ce^{4+} ions are doped into the lattice of perovskite.[42, 43] When the Ce molar fraction is larger than 0.2, the peak shifts back to 779.9 eV ($La_{0.6}Ce_{0.4}Fe_{0.4}Co_{0.6}O_3$) and the peak area decreases. It demonstrates that as the doping amount

of Ce further increasing, the valence of Co slightly ascends.

Figure 6 shows the O 1s XPS spectra of $La_{1-x}Ce_xFe_{1-y}Co_yO_3$ catalysts. The O 1s spectra have been divided into three components using the curve-fitting approach to get a relative content of different oxygen species. The detailed results are listed in Table 2. It can be concluded that the peaks at 533.1-533.4 eV are attributed to surface adsorbed molecular water, and the peaks at 513.1-531.4 eV are ascribed to the surface adsorbed oxygen species (O_{ads}). Another low BE peak at about 519.0 eV is due to the lattice oxygen species (O_{lat}).[43] For many oxidation reactions, the adsorbed oxygen species are very active at low temperatures and the area ratio of O_{ads}/O_{lat} is a sign to evaluate the oxidative performances of catalysts.[44] From Table 2, it can be found that the addition of Co in the B-site increases the O_{ads}/O_{lat} ratio, and the ratio increases with Co-substituted amounts ascending. This ratio further rises when La partly substituted by Ce, and it reaches the highest point when 30% Ce is doped. Obviously, the catalyst $La_{0.7}Ce_{0.3}Fe_{0.4}Co_{0.6}O_3$ possesses the largest amount of surface adsorbed oxygen species, which can accelerate the reaction during soot combustion.

O_2-TPD measurements were carried out to investigate the adsorption and activation of oxygen on the catalysts. The O_2-TPD curves of 3DOM $LaFeO_3$, $LaFe_{0.4}Co_{0.6}O_3$ and $La_{0.7}Ce_{0.3}Fe_{0.4}Co_{0.6}O_3$ are shown in Figure 7. There are three main oxygen desorption peaks for each sample, <150 ^oC, 150-550 ^oC, and >500 ^oC, which are ascribed to the physical adsorption oxygen species, surface active oxygen species and lattice oxygen species, respectively.[16, 45] The surface active oxygen species are very important for soot combustion because the reaction often takes place at this temperature range. After Co is introduced, the peak area between 150-550 ^oC increases. With the further doping of Ce in A-site, a further

increase in peak area is observed. At this point, both the substitution of Ce and Co can increase the amount of surface active oxygen species, and thus the catalytic activities for soot combustion can be improved. The results are consistent with those of O 1s XPS results.

The reducibility of the catalysts were characterized by H_2-TPR technique, as displays in Figure 8. For pure $LaFeO_3$ perovskite, only one reduction stage appears at about 414 ^oC, which can be ascribed to the reduction of Fe^{4+} to Fe^{3+}, while the Fe^{3+} cannot be further reduced under the experimental conditions.[46] The reduction temperature, as a sign of intrinsic oxygen reactivity, is the critical factor in the soot oxidation state. The lower reduction temperature indicates the higher catalytic activity for soot oxidation. As the Co-substitution increases, the reduction peak moves towards the lower temperature accordingly. This is due to the increased content of Co^{3+} in the perovskites.[47] When A-site La is further replaced by Ce, two new peaks between 310 ^oC and 550 ^oC emerge. According to the results of XRD and FT-IR, the lower reduction peak (310-370 ^oC) is attributed to the Co_3O_4 particles dispersed on the surface of the perovskite.[48] While the higher reduction peak (430-550 ^oC) is assigned to the outermost layers reduction of Ce^{4+} to Ce^{3+} in the CeO_2.[49] Meanwhile, the special oxygen storage ability of Ce doped into the perovskite may make the reduction peak remarkably shift to the lower temperature in perovskite.[30] When the content of Ce at A-site reaches up to 0.3, the reduction temperature is the lowest, which demonstrates that the $La_{0.7}Ce_{0.3}Fe_{0.4}Co_{0.6}O_3$ has the best reducibility among all the as-prepared catalysts. However, when excessive amount of Ce is added, all the reduction peaks slightly shift to the higher temperature owing to the increasing amount of impurity phases on the surface of perovskite.

3.2. Catalytic soot combustion over $La_{1-x}Ce_xFe_{1-y}Co_yO_3$ catalysts.

The above results of XRD and FT-IR characterization show that perovskite-type oxides are the major phases in the as-prepared catalysts, though a few CeO_2 and Co_3O_4 phases are also detected in Ce-substitution catalysts. According to the literature,[13, 50] perovskite oxides are believed to be the main active phases for soot combustion. The catalytic activities of 3DOM $La_{1-x}Ce_xFe_{1-y}Co_yO_3$ catalysts for soot oxidation under loose contact have been evaluated by homemade TPO device using NO/O_2 mixture as oxidizing agent and the results are shown in Figure 9 and Table 3. For comparison, the activities of particle catalysts with the same composition are also included. For soot combustion without catalyst, the T_{10}, T_{50}, and T_{90} are 500, 590, and 653 °C respectively, and the S_{CO2}^{m} is 63.2%. All the 3DOM catalysts are active in soot combustion with relatively low combustion temperature of soot and high selectivity of CO_2 (more than 96%). However, the particle catalysts show lower activities compared with the 3DOM catalysts in the same composition. The main reason is the difference in structure. Soot oxidation often occurs at three phase boundary among soot (solid phase), catalyst (solid phase) and gaseous reactants (gaseous phase).[13, 14] The contact conditions between soot and the catalysts play an important role in this kind of heterogeneous catalysis reactions. As shown in Figure 10, the soot particles can go inside the pores of 3DOM $La_{1-x}Ce_xFe_{1-y}Co_yO_3$ under loose contact. It means that the soot can be catalyzed both in the external surface and in the internal surface of the 3DOM catalysts. The improvement of effective contact area can further lower the soot combustion temperature, which demonstrates that the catalysts with 3DOM structure are more active than nanoparticle catalysts in soot combustion.

For 3DOM $LaFeO_3$ catalyst, the T_{50} of soot decreases to 478 °C and the combustion

temperature further declines monotonously along with the increase of Co-substitution. For soot combustion, the activity of $LaFeO_3$ is much lower than that of $LaCoO_3$, and thus substitution of Co for Fe can improve the activity of the perovskites. When the doping amount of Co increases to 0.6, the promotion effect on catalytic activity trends to flat. The above characterization results show that the substitution of Co destroys the well-ordered macropore structure. The fractured macropore skeletons pile up on the surface of the catalysts, just like the nanoparticles prepared by the citric acid-ligated combustion method.[51] The nanoparticle catalysts show relatively low activities than the corresponding 3DOM ones.[14, 52] As a result, the destruction of 3DOM structure caused by Co-substitution partly inhibits the further improvement of the catalytic activity.

After the introduction of Ce, the activity of the catalyst is enhanced with the decrease of soot combustion temperature. Based upon above characterization results, the improvement of the activity for soot combustion can be assigned to the following two aspects. Firstly, the introduction of Ce can avoid the collapse of 3DOM structure. The interpenetrating well-ordered macroporous structure permits soot particles to go through the structure with less diffusion resistance and the available active sites of the catalysts will be increased remarkably. The maintained 3DOM structure can improve the activity of catalysts from the structure advantage. Secondly, as revealed by O 1s XPS and O_2-TPD results, Ce-doped samples possess more surface adsorbed oxygen species which facilitate the transferring of oxygen species during soot combustion. Meanwhile, the introduction of Ce also improves the reducibility of the catalyst, which accelerates the redox circulation during soot combustion. The improvement of intrinsic property of the catalyst also enhances the catalytic activity.

However, the excess addition of Ce decreases the activity due to the formation of CeO_2 and Co_3O_4 impurities as the 3DOM CeO_2 and Co_3O_4 exhibit lower catalytic activities compared with the 3DOM $La_{1-x}Ce_xFe_{0.4}Co_{0.6}O_3$ ($0 \geqslant x \geqslant 0.4$) catalysts. Among all the catalysts, the highest activity is obtained when the doping amount of Ce is 0.3 and the corresponding T_{10}, T_{50}, T_{90}, and S_{CO2}^{m} are 330, 410, 473 °C, and 97.2 %, respectively.

The catalytic activities of 3DOM $La_{0.7}Ce_{0.3}Fe_{0.4}Co_{0.6}O_3$ for soot combustion in the absence of NO were also evaluated by TPO method and the results are shown in Figure 11. As shown in Figure 11, the catalytic performance of 3DOM $La_{0.7}Ce_{0.3}Fe_{0.4}Co_{0.6}O_3$ in the absence of NO is lower than that in the presence of NO, with the T_{10}, T_{50} and T_{90} of soot increasing from 339, 410, and 473 °C to 378, 457, and 520 °C, respectively. In order to study the effect of NO in the reaction, NO oxidation experiment was also carried out. Figure 12 shows the NO_2 concentration profile during NO oxidation over 3DOM $La_{0.7}Ce_{0.3}Fe_{0.4}Co_{0.6}O_3$ catalyst. For comparison, the profile without catalyst is also included. As shown in Figure 12, NO cannot convert to NO_2 without the help of catalyst as the outlet NO_2 concentration is low. After 3DOM $La_{0.7}Ce_{0.3}Fe_{0.4}Co_{0.6}O_3$ catalyst is added, the outlet NO_2 concentration increases remarkably at first, and then decreases with the temperature increasing. The corresponding temperature of maximum NO_2 concentration is about 380 °C, which is accorded with the soot combustion temperature. NO_2, as a strong oxidant, can oxidize soot much more effective than O_2.[53] It can be concluded that the soot is oxidized by NO_2 converted from NO, rather than directly oxidized by O_2 during soot combustion.

Table 4 lists the relevant results reported in literature. As seen in Table 4, many researches focus on perovskite-type catalysts on soot combustion. Among them, the

perovskite-type catalysts with noble metal (Entry 1, 2)[16, 54] or alkali metal (Entry 3, 4)[14, 32] show the higher activities for soot combustion than other catalysts. The component of reactant gas and the contact between soot and catalyst also affect the soot combustion temperature. Considering the factors above, the catalysts in this work have relatively high catalytic activities compared with the similar component of catalyst (Entry 5-7).[28, 55, 56]

4. Conclusions

A series of 3DOM $La_{1-x}Ce_xFe_{1-y}Co_yO_3$ (x=0-0.4, y=0-0.6) perovskite catalysts were successfully prepared by colloidal crystal templating method and applied for soot combustion. When Fe is partly substituted by Co, the redox property and the activity of catalyst improve obviously. While with the excess addition of Co, the 3DOM structure is partly destroyed and further improvement of catalytic activity is inhibited. The doping of Ce in A-site avoids the collapse of macroporous by the relatively low solidification temperature of Ce, and the redox property of the catalyst is also enhanced by the special oxygen storage ability of Ce. Nevertheless, the formation of CeO_2 and Co_3O_4 impurities will occur at high Ce content owing to the distortion and the contraction of perovskite lattice. Among all the prepared catalysts, the 3DOM $La_{0.7}Ce_{0.3}Fe_{0.4}Co_{0.6}O_3$ catalyst shows the highest catalytic activity for soot combustion with the lowest T_{50} at 410 ^oC under loose contact.

Acknowledgements

The work was supported by R&D Project for Environmental Protection of Jiangsu of China (NO. 2015002), the Foundation from State Key Laboratory of Materials-Oriented Chemical Engineering, Nanjing Tech University (ZK201305) and Research and Innovation

Training Project for Graduate in General Universities of Jiangsu Province (No. KYZZ15_0227).

References:

1 T. W. Hesterberg, C. M. Long, W. B. Bunn, C. A. Lapin, R. O. Mcclellan, P. A. Valberg, *Inhal. Toxicol.*, 2012, **24**, 1-45.

2 M. V. Twigg, M. V. Twigg, *Appl. Catal. B*, 2007, **70**, 2-15.

3 A. Hernández-Giménez, D. Castelló, A. Bueno-López, *Chem. Pap.*, 2014, **68**, 1154-1168.

4 X. Niu, L. Zhou, X. Hu, W. Han, *RSC Adv.*, 2015, **5**. 52595-52601.

5 L. Shuang, X. Wu, W. Duan, L. Min, J. Fan, *Appl. Catal. B*, 2013, **138**, 199-211.

6 R. Matarrese, L. Castoldi, N. Artioli, E. Finocchio, G. Busca, L. Lietti, *Appl. Catal. B*, 2014, **144**, 783-791.

7 B. Azambre, S. Collura, P. Darcy, J. M. Trichard, P. D. Costa, A. García-García, A. Bueno-López, *Fuel Process. Technol.*, 2011, **92**, 363-371.

8 S. Fang, L. Wang, Z. Sun, N. Feng, C. Shen, P. Lin, H. Wan, G. Guan, *Catal. Commun.*, 2014, **49**, 15-19.

9 W. Hong, L. Jian, Z. Zhen, Y. Wei, C. Xu, *Catal. Today*, 2012, **184**, 288-300.

10 J. Zhu, H. Li, L. Zhong, P. Xiao, X. Xu, X. Yang, Z. Zhao, J. Li, *ACS Catal.*, 2014, **4**, 2917-2940.

11 G. Pecchi, R. Dinamarca, C. M. Campos, X. Garcia, R. Jimenez, J. L. G. Fierro, *Ind. Eng. Chem. Res*, 2014, **53**, 10090-10096.

12 G. Pecchi, M. G. Jiliberto, E. J. Delgado, L. E. Cadús, J. L. G. Fierro, *J. Chem. Technol.*

Biot., 2011, **86**, 1067-1073.

13 Z. Li, M. Meng, Y. Zha, F. Dai, T. Hu, Y. Xie, J. Zhang, *Appl. Catal. B*, 2012, **282**, 65-74.

14 J. Xu, J. Liu, Z. Zhao, C. Xu, J. Zheng, A. Duan, G. Jiang, *J. Catal.*, 2011, **282**, 1-12.

15 M. Sadakane, T. Asanuma, J. Kubo, W. Ueda, *Chem. Mater.*, 2005, **17**, 3546-3551.

16 Y. Wei, J. Liu, Z. Zhao, Y. Chen, C. Xu, A. Duan, G. Jiang, H. He, *Angew. Chem. Int. Edit.*, 2011, **50**, 2326-2329.

17 X. Yu, Z. Zhao, Y. Wei, J. Liu, J. Li, A. Duan, G. Jiang, *RSC Adv.*, 2015, **5**, 49780-49790.

18 J. Ma, Y. Ning, C. Gong, G. Xue, G. Fan, *RSC Adv.*, 2015, **5**, 53441-53447.

19 S. Xie, H. Dai, J. Deng, Y. Liu, H. Yang, Y. Jiang, W. Tan, A. Ao, G. Guo, *Nanoscale*, 2013, **5**, 11207-11219.

20 K. Zhao, F. He, Z. Huang, A. Zheng, H. Li, Z. Zhao, *Int. J. Hydrogen Energ.*, 2014, **39**, 3243-3252.

21 J. Xu, Z. Wang, D. Xu, F. Meng, X. Zhang, *Energ. Environ. Sci.*, 2014, **7**, 2213-2219.

22 M. Sadakane, K. Sasaki, H. Nakamura, T. Yamamoto, W. Ninomiya, W. Ueda, *Langmuir*, 2012, **28**, 17766-17770.

23 J. Xu, J. Liu, Z. Zhao, J. Zheng, G. Zhang, A. Duan, G. Jiang, *Catal. Today*, 2010, **153**, 136-142.

24 M. Kurnatowska, W. Mista, P. Mazur, L. Kepinski, *Appl. Catal. B*, 2014, **148**, 123-135.

25 H. Zhang, F. Gu, Q. Liu, J. Gao, L. Jia, T. Zhu, Y. Chen, Z. Zhong, F. Su, *RSC Adv.*, 2014, **4**, 14879-14889.

26 Y. Wei, Z. Zhao, X. Yu, B. Jin, J. Liu, C. Xu, A. Duan, G. Jiang, S. Ma, *Catal. Sci. Technol.*, 2013, **3**, 2958-2970.

27 S. Quiles-Díaz, J. Giménez-Mañogil, A. García-García, *RSC Adv.*, 2015, **5**, 17018-17029.

28 S. Wu, C. Song, F. Bin, G. Lv, J. Song, C. Gong, *Mater. Chem. Phys.*, 2014, **148**, 181-189.

29 X. Xiang, L. Zhao, B. Teng, J. Lang, X. Hu, T. Li, Y. Fang, M. Luo, J. Lin, *Appl. Surf. Sci.*, 2013, **276**, 328-332.

30 R. Zhang, N. Luo, B. Chen, S. Kaliaguine, *Energ. Fuel.*, 2010, **24**, 3719-3726.

31 H. Arandiyan, H. Dai, J. Deng, Y. Liu, B. Bai, Y. Wang, X. Li, S. Xie, J. Li, *J. Catal.*, 2013, **307**, 327-339.

32 B. Feng, C. Song, G. Lv, J. Song, C. Gong, Q. Huang, *Ind. Eng. Chem. Res.*, 2011, **50**, 6660-6667.

33 X. Meng, F. He, X. Shen, J. Xiang, P. Wang, *Ind. Eng. Chem. Res.*, 2011, **50**, 11037-11042.

34 X. Guo, M. Meng, F. Dai, Q. Li, Z. Zhang, Z. Jiang, S. Zhang, Y. Huang, *Appl. Catal. B*, 2013, **142-143**, 278-289.

35 K. M. Parida, K. H. Reddy, S. Martha, D. P. Das, N. Biswal, *Int. J. Hydrogen Energ.*, 2010, **35**, 12161-12168.

36 H. Wu, R. Hu, T. Zhou, C. Li, W. Meng, J. Yang, *CrystEngComm*, 2015, **17**, 3859-3865.

37 M. Surendar, T. V. Sagar, B. H. Babu, N. Lingaiah, K. R. Rao, P. S. Prasad, *RSC Adv.*, 2015, **5**, 45184-45193.

38 E. V. Makshina, N. S. Nesterenko, S. Siffert, E. A. Zhilinskaya, A. Aboukais, B. V. Romanovsky, *Catal. Today*, 2008, **131**, 427-430.

39 C. Zhang, W. Hua, C. Wang, Y. Guo, Y. Guo, G. Lu, A. Baylet, A. Giroir-Fendler, *Appl. Catal. B*, 2013, **134**, 310-315.

40 M. Ghasdi, H. Alamdari, S. Royer, A. Adnot, *Sensor. Actuat. B*, 2011, **156**, 147-155.

41 R. Tan, Y. Zhu, *Appl. Catal. B*, 2005, **58**, 61-68.

42 Y. Luo, K. Wang, Q. Chen, Y. Xu, H. Xue, Q. Qian, *J. Hazard. Mater.*, 2015, **296**, 17-22.

43 Y. Wen, C. Zhang, H. He, Y. Yu, Y. Teraoka, *Catal. Today*, 2007, **126**, 400-405.

44 G. Zou, Y. Xu, S. Wang, M. Chen, W. Shangguan, *Catal. Sci. Technol.*, 2015, **5**, 1084-1092.

45 S. Sun, L. Yang, G. Pang, S. Feng, *Appl. Catal. A*, 2011, **401**, 199-203.

46 N. A. Merino, B. P. Barbero, P. Ruiz, L. E. Cadús, *J. Catal.*, 2006, **240**, 245-257.

47 N. Russo, S. Furfori, D. Fino, G. Saracco, V. Specchia, *Appl. Catal. B*, 2008, **83**, 85-95.

48 H. Wu, G. Pantaleo, G. Di Carlo, S. Guo, G. Marcì, P. Concepción, A. M. Venezia, L. F. Liotta, *Catal. Sci. Technol.*, 2015, **5**, 1888-1901.

49 C. He, Y. Yu, C. Chen, L. Yue, N. Qiao, Q. Shen, J. Chen, Z. Hao, *RSC Adv.*, 2013, **3**, 19639-19656.

50 X. Li, Y. Dong, H. Xian, W. Y. Hernández, M. Meng, H. Zou, A. Ma, T. Zhang, Z. Jiang, N. Tsubaki, *Energ. Environ. Sci.*, 2011, **4**, 3351-3354.

51 Z. Li, M. Meng, Q. Li, Y. Xie, T. Hu, J. Zhang, *Chem. Eng. J.*, 2010, **164**, 98-105.

52 Y. Wei, Z. Zhao, T. Li, J. Liu, A. Duan, G. Jiang, *Appl. Catal. B*, 2014, **146**, 57-70.

53 K. Leistner, A. Nicolle, P. Da Costa, *J. Phys. Chem. C*, 2012, **116**, 4642-4654.

54 K. Wang, L. Qian, L. Zhang, H. Liu, Z. Yan, *Catal. Today*, 2010, **158**, 423-426.

55 R. Zhang, N. Luo, B. Chen, S. Kaliaguine, *Energ. Fuel.*, 2010, **24**, 3719-3726.

56 Z. Liu, Z. Hao, H. Zhang, Y. Zhuang, *J. Chem. Technol. Biot.*, 2002, **77**, 800-804.

Captions for Tables

Table 1. Crystal sizes and BET surface areas of 3DOM $La_{1-x}Ce_xFe_{1-y}Co_yO_3$ catalysts

Table 2. Binding energies of O1s and the percentages of different kinds of surface oxygen species for 3DOM $La_{1-x}Ce_xFe_{1-y}Co_yO_3$ catalysts

Table 3. The temperatures and the selectivities to CO_2 for soot combustion over without catalyst, the particle $La_{1-x}Ce_xFe_{1-y}Co_yO_3$ and 3DOM $La_{1-x}Ce_xFe_{1-y}Co_yO_3$, CeO_2, Co_3O_4

Table 4. The catalytic activities for soot combustion over perovskite-type catalysts in literatures

Table 1. Crystal sizes and BET surface areas of 3DOM $La_{1-x}Ce_xFe_{1-y}Co_yO_3$ catalysts

Catalyst	2θ (°)	D (nm)	BET (m^2/g)
$LaFeO_3$	32.18	24.2	21.7
$LaFe_{0.8}Co_{0.2}O_3$	32.34	24.0	21.4
$LaFe_{0.6}Co_{0.4}O_3$	32.52	23.8	19.8
$LaFe_{0.4}Co_{0.6}O_3$	32.70	22.9	18.5
$La_{0.9}Ce_{0.1}Fe_{0.4}Co_{0.6}O_3$	32.66	22.7	18.9
$La_{0.8}Ce_{0.2}Fe_{0.4}Co_{0.6}O_3$	32.62	21.0	20.5
$La_{0.7}Ce_{0.3}Fe_{0.4}Co_{0.6}O_3$	32.54	19.8	22.5
$La_{0.6}Ce_{0.4}Fe_{0.4}Co_{0.6}O_3$	32.42	18.4	22.4

Table 2. Binding energies of O1s and the percentages of different kinds of surface oxygen species for 3DOM $La_{1-x}Ce_xFe_{1-y}Co_yO_3$ catalysts.

Catalyst	H_2O		O_{ads}		O_{lat}		O_{ads}/O_{lat}
	BE(ev)	Area	BE(ev)	Area	BE(ev)	Area	
$LaFeO_3$	533.3	392.4	531.2	7247.6	528.9	9244.7	0.78
$LaFe_{0.8}Co_{0.2}O_3$	533.4	491.1	531.2	7397.9	529.1	8982.7	0.82
$LaFe_{0.6}Co_{0.4}O_3$	533.3	392.4	531.3	7559.4	528.9	8877.3	0.85
$LaFe_{0.4}Co_{0.6}O_3$	533.3	713.9	531.3	8105.7	528.9	9093.3	0.89
$La_{0.9}Ce_{0.1}Fe_{0.4}Co_{0.6}O_3$	533.1	854.6	531.1	7876.1	528.9	9386.8	0.84
$La_{0.8}Ce_{0.2}Fe_{0.4}Co_{0.6}O_3$	533.3	638.4	531.2	8426.6	529.0	9404.8	0.90
$La_{0.7}Ce_{0.3}Fe_{0.4}Co_{0.6}O_3$	533.3	747.7	531.4	8477.5	529.0	9039.8	0.94
$La_{0.6}Ce_{0.4}Fe_{0.4}Co_{0.6}O_3$	533.1	759.8	531.2	6107.7	528.7	9594.4	0.64

Table 3. The temperatures and the selectivities to CO_2 for soot combustion over without catalyst, the particle $La_{1-x}Ce_xFe_{1-y}Co_yO_3$ and 3DOM $La_{1-x}Ce_xFe_{1-y}Co_yO_3$, CeO_2, Co_3O_4

Catalyst	T_{10} (°C)	T_{50} (°C)	T_{90} (°C)	S^m_{CO2} (%)
Soot (without catalyst)	500	590	653	63.2
$LaFeO_3$ (particle)	440	512	574	95.2
$LaFeO_3$ (3DOM)	405	478	543	97.2
$LaFe_{0.8}Co_{0.2}O_3$ (particle)	419	494	560	96.2
$LaFe_{0.8}Co_{0.2}O_3$ (3DOM)	389	460	525	96.3
$LaFe_{0.6}Co_{0.4}O_3$ (particle)	398	475	541	95.8
$LaFe_{0.6}Co_{0.4}O_3$ (3DOM)	370	444	508	96.9
$LaFe_{0.4}Co_{0.6}O_3$ (particle)	379	459	522	96.1
$LaFe_{0.4}Co_{0.6}O_3$ (3DOM)	360	438	499	96.1
$La_{0.9}Ce_{0.1}Fe_{0.4}Co_{0.6}O_3$ (particle)	376	448	514	95.1
$La_{0.9}Ce_{0.1}Fe_{0.4}Co_{0.6}O_3$ (3DOM)	351	422	485	97.3
$La_{0.8}Ce_{0.2}Fe_{0.4}Co_{0.6}O_3$ (particle)	372	442	500	96.3
$La_{0.8}Ce_{0.2}Fe_{0.4}Co_{0.6}O_3$ (3DOM)	345	414	477	97.0
$La_{0.7}Ce_{0.3}Fe_{0.4}Co_{0.6}O_3$ (particle)	369	437	495	95.2
$La_{0.7}Ce_{0.3}Fe_{0.4}Co_{0.6}O_3$ (3DOM)	339	410	473	97.2
$La_{0.6}Ce_{0.4}Fe_{0.4}Co_{0.6}O_3$ (particle)	404	478	540	95.8
$La_{0.6}Ce_{0.4}Fe_{0.4}Co_{0.6}O_3$ (3DOM)	377	446	511	96.9
CeO_2 (3DOM)	380	463	529	96.8
Co_3O_4 (3DOM)	374	451	516	97.0

Table 4. The catalytic activities for soot combustion over perovskite-type catalysts in literatures

Entry	Catalyst	Reactant gas	Contact	T_m or T_{50} or T_p (^oC)	References
1	$La_{0.7}Ag_{0.3}MnO_3$	2000 ppm NO+5% O_2	loose	401	54
2	$Au_{0.04}/LaFeO_3$(3DOM)	2000 ppm NO+5% O_2	loose	368	16
3	$La_{0.9}K_{0.1}CoO_3$(3DOM)	2000 ppm NO+5% O_2	loose	378	14
4	$La_{0.6}K_{0.4}CoO_3$	800 ppm NO+ 10% O_2	loose	382	32
5	$La_{0.8}Ce_{0.2}Mn_{0.7}Co_{0.3}O_3$	Air	tight	424	28
6	$La_{0.7}Ce_{0.4}Fe_{0.5}Co_{0.5}O_3$	10% O_2	loose	433	56
7	$LaCe_{0.2}CoO_3$	10% O_2	tight	435	55
8	$La_{0.7}Ce_{0.3}Fe_{0.4}Co_{0.6}O_3$(3DOM)	500 ppm NO+5% O_2	loose	410	This work

Captions for Figures

Figure 1. SEM images of 3DOM $La_{1-x}Ce_xFe_{1-y}Co_yO_3$ catalysts: (a) $LaFeO_3$; (b) $LaFe_{0.8}Co_{0.2}O_3$; (c) $LaFe_{0.6}Co_{0.4}O_3$; (d) $LaFe_{0.4}Co_{0.6}O_3$; (e) $La_{0.9}Ce_{0.1}Fe_{0.8}Co_{0.2}O_3$; (f) $La_{0.8}Ce_{0.2}Fe_{0.8}Co_{0.2}O_3$; (g) $La_{0.7}Ce_{0.3}Fe_{0.8}Co_{0.2}O_3$; (h) $La_{0.6}Ce_{0.4}Fe_{0.8}Co_{0.2}O_3$

Figure 2. XRD patterns of 3DOM $La_{1-x}Ce_xFe_{1-y}Co_yO_3$ catalysts: full patterns (a); enlarged reflections (b)

Figure 3. FT-IR spectra of 3DOM $La_{1-x}Ce_xFe_{1-y}Co_yO_3$ catalysts

Figure 4. UV-Vis spectroscopy of 3DOM $LaFeO_3$, $LaFe_{0.4}Co_{0.6}O_3$ and $La_{0.7}Ce_{0.3}Fe_{0.4}Co_{0.6}O_3$

Figure 5. XPS spectra of Ce 3d (A) and Co 2p (B) regions for the 3DOM $La_{1-x}Ce_xFe_{0.4}Co_{0.6}O_3$

Figure 6. XPS spectra of O 1s for 3DOM $La_{1-x}Ce_xFe_{1-y}Co_yO_3$ catalysts

Figure 7. O_2-TPD curves of 3DOM $LaFeO_3$, $LaFe_{0.4}Co_{0.6}O_3$ and $La_{0.7}Ce_{0.3}Fe_{0.4}Co_{0.6}O_3$

Figure 8. H_2-TPR profiles of 3DOM $La_{1-x}Ce_xFe_{1-y}Co_yO_3$ catalysts

Figure 9. The conversion rate of soot over 3DOM $La_{1-x}Ce_xFe_{1-y}Co_yO_3$ ($0\leq x\leq 0.4$, $0\leq y\leq 0.6$) catalysts

Figure 10. SEM image of 3DOM $La_{0.7}Ce_{0.3}Fe_{0.4}Co_{0.6}O_3$ catalyst and soot under loose contact

Figure 11. The soot conversion over 3DOM $La_{0.7}Ce_{0.3}Fe_{0.4}Co_{0.6}O_3$ in the presence and absence of NO

Figure 12. The outlet NO_2 ion current curves during NO oxidation process

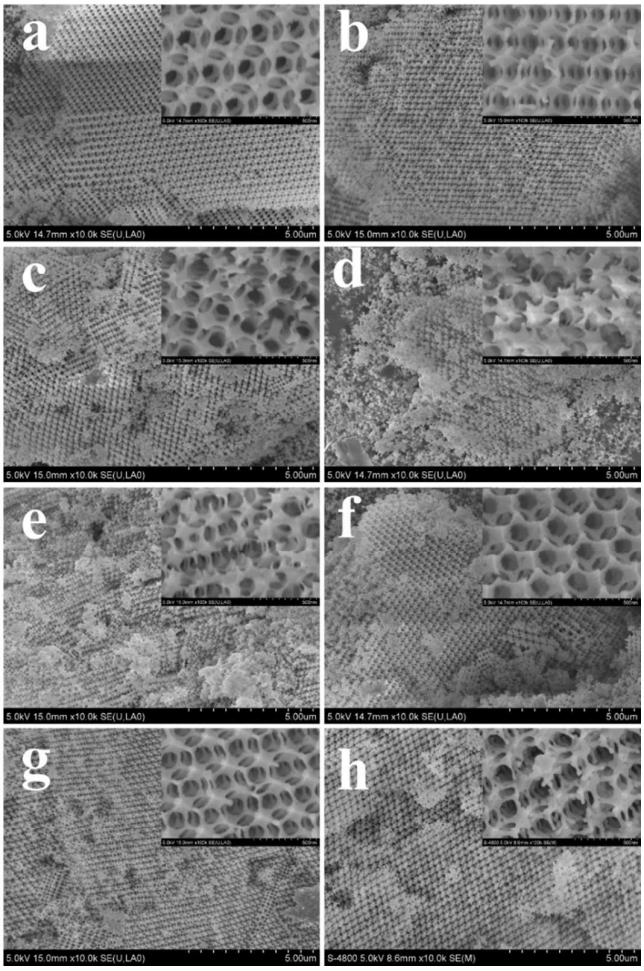

Figure 1. SEM images of 3DOM $La_{1-x}Ce_xFe_{1-y}Co_yO_3$ catalysts: (a) $LaFeO_3$; (b) $LaFe_{0.8}Co_{0.2}O_3$; (c) $LaFe_{0.6}Co_{0.4}O_3$; (d) $LaFe_{0.4}Co_{0.6}O_3$; (e) $La_{0.9}Ce_{0.1}Fe_{0.8}Co_{0.2}O_3$; (f) $La_{0.8}Ce_{0.2}Fe_{0.8}Co_{0.2}O_3$; (g) $La_{0.7}Ce_{0.3}Fe_{0.8}Co_{0.2}O_3$; (h) $La_{0.6}Ce_{0.4}Fe_{0.8}Co_{0.2}O_3$

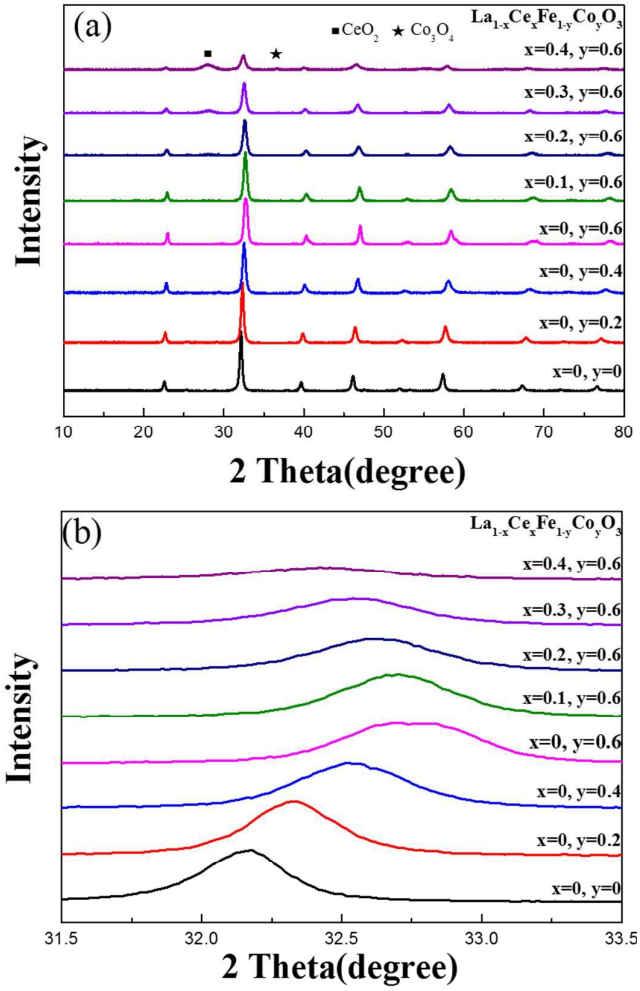

Figure 2. XRD patterns of 3DOM $La_{1-x}Ce_xFe_{1-y}Co_yO_3$ catalysts: full patterns (a); enlarged reflections (b)

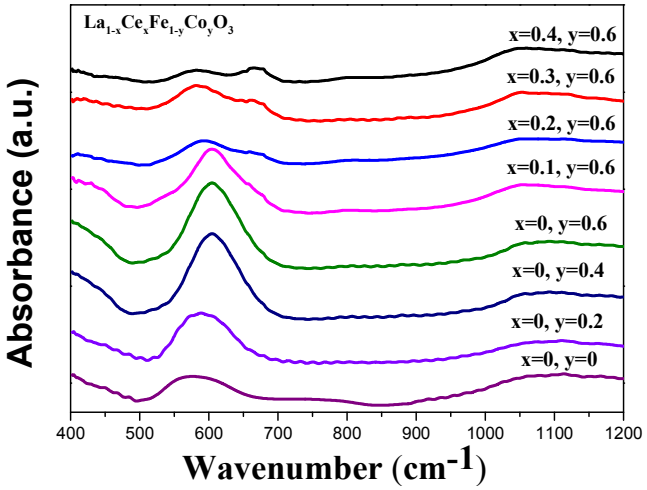

Figure 3. FT-IR spectra of 3DOM $La_{1-x}Ce_xFe_{1-y}Co_yO_3$ catalysts

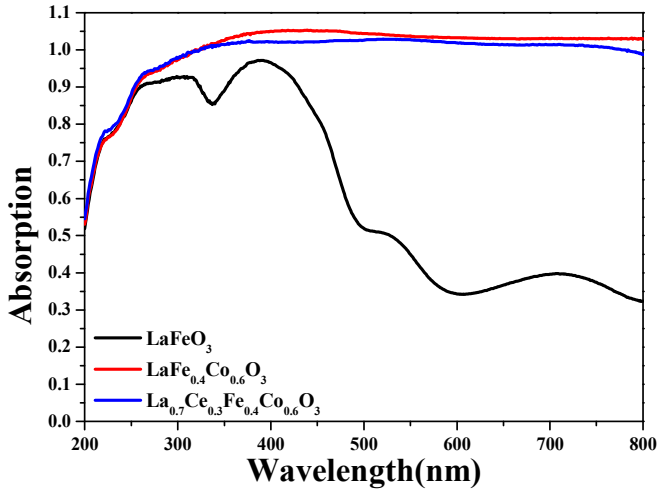

Figure 4. UV-Vis spectroscopy of 3DOM $LaFeO_3$, $LaFe_{0.4}Co_{0.6}O_3$ and $La_{0.7}Ce_{0.3}Fe_{0.4}Co_{0.6}O_3$

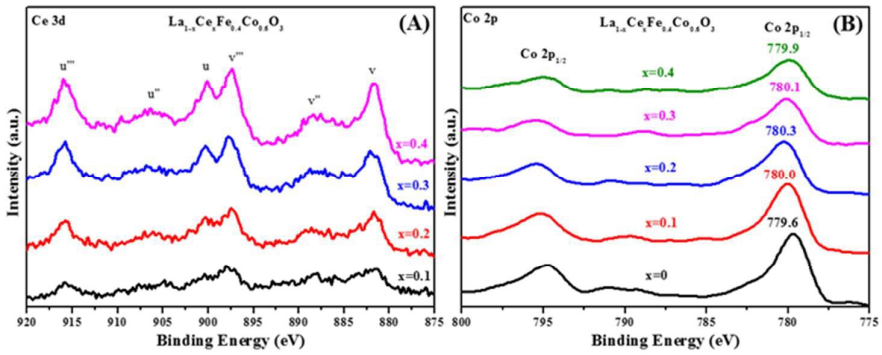

Figure 5. XPS spectra of Ce 3d (A) and Co 2p (B) regions for the 3DOM $La_{1-x}Ce_xFe_{0.4}Co_{0.6}O_3$

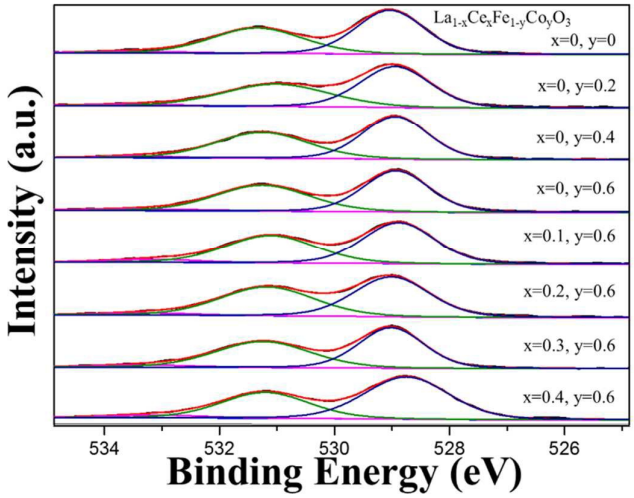

Figure 6. XPS spectra of O1s for 3DOM $La_{1-x}Ce_xFe_{1-y}Co_yO_3$ catalysts

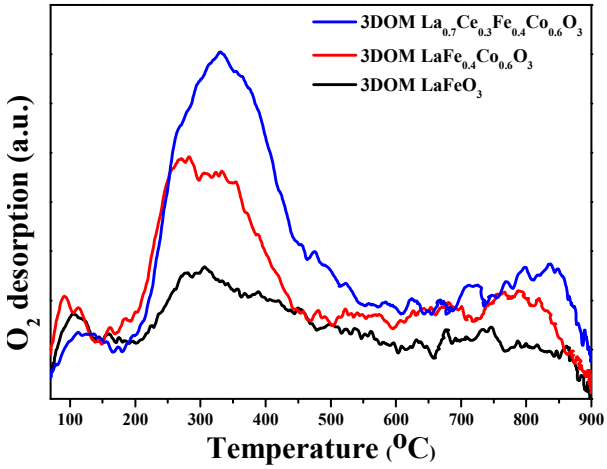

Figure 7. O_2-TPD curves of 3DOM $LaFeO_3$, $LaFe_{0.4}Co_{0.6}O_3$ and $La_{0.7}Ce_{0.3}Fe_{0.4}Co_{0.6}O_3$

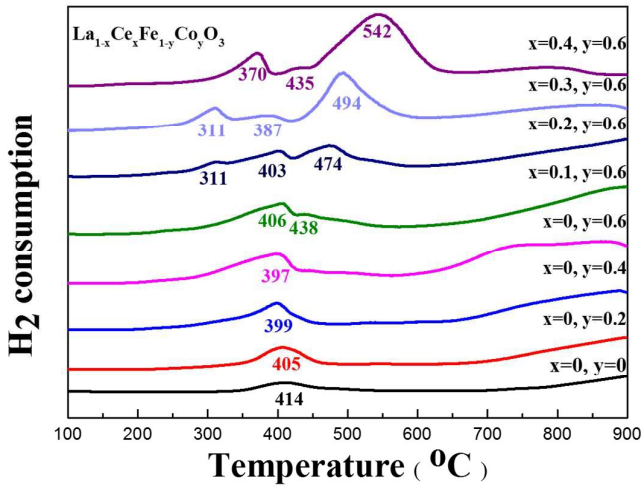

Figure 8. H_2-TPR profiles of 3DOM $La_{1-x}Ce_xFe_{1-y}Co_yO_3$ catalysts

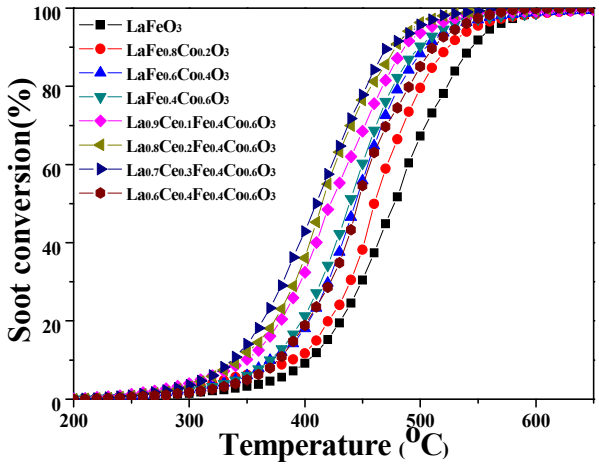

Figure 9. The conversion rate of soot over 3DOM $La_{1-x}Ce_xFe_{1-y}Co_yO_3$ ($0 \le x \le 0.4$, $0 \le y \le 0.6$) catalysts

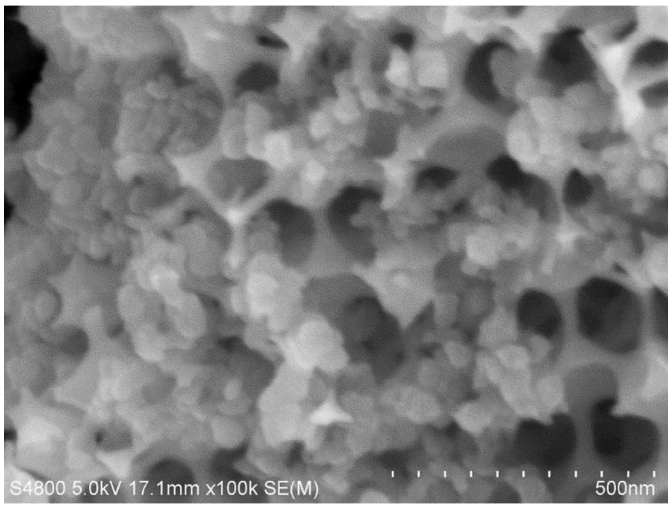

Figure 10. SEM image of 3DOM $La_{0.7}Ce_{0.3}Fe_{0.4}Co_{0.6}O_3$ catalyst and soot under loose contact

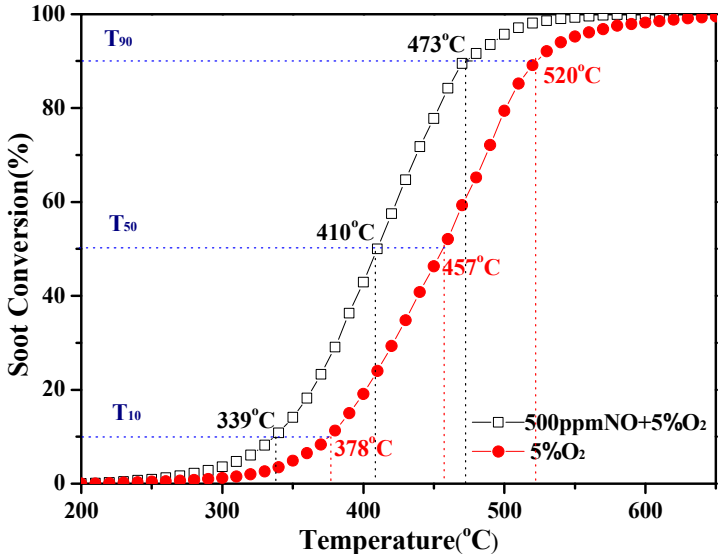

Figure 11. The soot conversion over 3DOM $La_{0.7}Ce_{0.3}Fe_{0.4}Co_{0.6}O_3$ in the presence and absence of NO

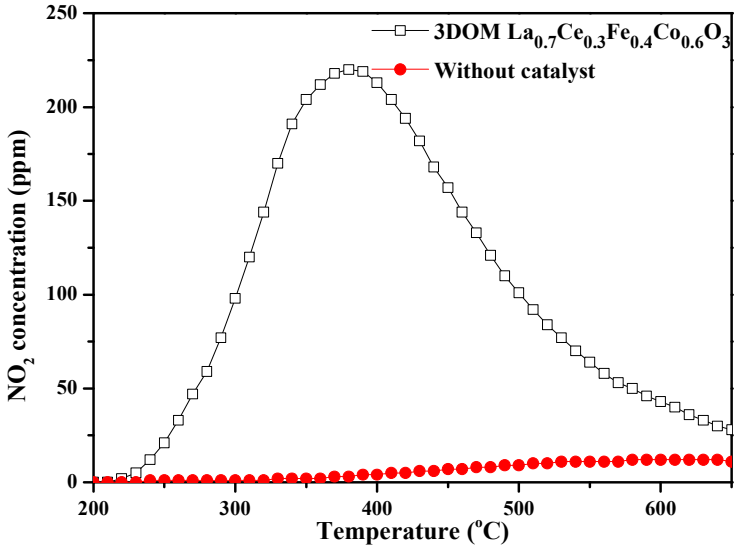

Figure 12. The outlet NO_2 ion current curves during NO oxidation process